CrossMark

Evaluation of the reaction mechanism for photocatalytic degradation of organic pollutants with MIL-88A/BiOI structure under visible light irradiation

Sepideh Gholizadeh Khasevani[1] · Mohammad Reza Gholami[1] (ID)

Abstract

In this study, we synthesized novel visible light photocatalyst MIL-88A/BiOI using depositing BiOI particles on the surface of a metal–organic framework (MIL-88A). Photocatalytic application of binary composite MIL-88A/BiOI was obtained by discoloration of Methylene Blue (MB) and Acid Blue 92 (AB92) in aqueous solution under visible light source. The photodegradation experiments for treating organic dyes show that the MIL-88A/BiOI heterojunction structure possess a higher rate for decomposition of dyes due to the decreased aggregation of the BiOI nanoparticles, effective charge carrier separation and the synergistic effect between MIL-88A and BiOI samples as a heterojunction. Also, the MIL-88A/BiOI structure shows better photocatalytic degradation performance for anionic dyes (AB92) than for a cationic dye (MB). It was further found that $^\bullet OH$ and $^\bullet O_2^-$ radicals were the most important species responsible for the photodegradation test.

Keywords Visible light-driven · Photocatalyst · MIL-88A metal organic framework · BiOI

Introduction

In recent years, organic dyes and toxic organic structures such as phenol and bacteria have become a most important global dilemma, because these toxic organic pollutants can reduce water quality and cause serious health issues. Various physical, chemical, and biological methods have been suggested to decompose organic pollutants, but these methods are usually expensive or require advanced technical instruments. Semiconductor-based photocatalysts have attracted wide interests in resolving these problems caused via advanced oxidation processes (AOPs) [1–3]. In

---

✉ Mohammad Reza Gholami
gholami@sharif.edu

1 Sharif University of Technology, Tehran, Iran

recent years, the different types of semiconductor components such as metal oxide [4], oxyacid [5], sulfides [6], nitrides [7] and bismuth-based materials Bi_2O_3, BiOX (X = Cl, Br, I), $BiVO_4$, Bi_2WO_6, Bi_2MoO_6, etc. have been explored as photocatalysts [8–10]. Among the single semiconductor-based bismuth-based compounds, bismuth oxyhalides (BiOX) with tetragonal structures and great electrical and optical properties exhibit excellent photocatalytic performances under visible light irradiation [11–13]. Bismuth oxyiodine (BiOI) structure, owing to its narrow optical gap (1.77 eV), is active in solar light irradiation, but the basic problem for this semiconductor is the high measured recombination rate of e^-/h^+ pairs [14, 15].

Therefore, the experimental results of a single semiconductor displayed many restrictions in photocatalytic application, such as the high recombination rate of photogenerated electron–hole pairs and limited visible-light response for wide band-gap semiconductors [16–18]. To overcome this problem, many promising strategies including doping with ions [19] and coupling with other semiconductors [20] have been done to suppress the charge carrier recombination, reduce the band gap and extend the absorption band for the enhancement of the photocatalytic activity [21, 22]. Recently, many of heterojunction-type semiconductors as visible light-driven photocatalysts such as C_3N_4-Bi_2WO_6 [23], HKUST-1@Ag-Ag_3PO_4 [24], $ZnFe_2O_4$/BiOI [25], Bi_2S_3/BiOI [26], p-BiOI/n-TiO_2 [27] and MoS_2/BiOI/AgI [28] have been fabricated and their photocatalytic activities have been studied. The BiOX coupling with suitable semiconductor materials has resulted in enhanced photocatalytic performance because of the prolonged lifetime and low recombination rate of carriers. Furthermore, the nanostructured metal–organic framework (MOF) has been affirmed to use in combination with BiOI to fabricate the visible light-driven photocatalyst [29–31].

MOFs are a new category of porous hybrid materials comprised of inorganic and organic materials like metal-oxo clusters and ligand, respectively. They possess exclusive features such as high specific surface areas, diverse composition and a controllable porous structure [32–34]. Consequently, MOFs have been widely used in gas capture and storage [35], biological medicine [36], sensor devices [37], chemical separation and purification [38] and catalysis [39, 40]. In recent years, MOFs have been used as sacrificial templates/precursors in synthesis of metal oxides such as CuO [41, 42], Cu_2O [43], CeO_2 [44, 45], Fe_2O_3 [46, 47] and Mn_2O_3 [48] for CO oxidation, hydrogen generation and the chemical oxidation process in water. Furthermore, the suitable band gap of MOF is related to the HOMO–LUMO gap which allows MOFs to be offered as promising materials in the photocatalysis field [49–51].

MOFs are generally microporous materials with high surface area compared to other supports like silica and polymers. Among MOF structures, Fe-containing MOFs using Fe_3-μ_3-oxo clusters with different organic linkers as photocatalyst reduce recombination and enhance photocatalytic performances [52–54]. In this case study, we reported a new type of Fe-containing MOF (MIL-88A) with large volume swelling to the polar solvent; it is built of trimers of Fe(III) octahedral connected by fumarate dianions and shows a framework structure with open channels that run along the the c axis. It is noteworthy that MIL-88A shows a reversible doubling (approximately 85%) of its cell volume while retaining its open-framework topology. It is obvious that photocatalytic

activity is related to the reaction on the surface in which the reactant needs to be preab-sorbed on the surface of the photocatalyst. Thus, MIL-88A by a large swelling effect is very considerable for mass transport in photoactivity [52]. In this work, a novel binary structure of MIL-88A/BiOI photocatalyst has been fabricated. The photocatalytic per-formance based on degradation of AB92 and MB under visible light irradiation is stud-ied, and also discussed is the scrupulously practical process and its characterizations.

Experimental

Characterization of photocatalysts

Fourier transform infrared spectroscopy was recorded with an ABB BOMER MB series spectrophotometer. X-ray diffraction (XRD) patterns of as-synthesized samples were obtained using a Philips X'pert instrument operating with Cu Kα ($\lambda = 0.15406$ nm) radiation at 40 kV/40 mA. Surface morphological analysis (SEM) and transmission electron microscopy (TEM) were done using a Philips XL30 field-emission scanning electron microscope and Philips CM30 device. Electrochemical impedance spectros-copy (EIS) were conducted using an Autolab potentiostat/galvanostat (EG&G model 263A, USA). UV–Vis absorption spectra for the obtained materials were determined using an UV–Vis spectrophotometer (GBC Cintra 40). The Brunauer–Emmett–Teller (BET) specific surface area was calculated by applying the BET equation. The pore size distribution was obtained by the Barret−Joyner−Halenda (BJH) method. The pho-toluminescence (PL) spectra of the samples were studied using a Varian Cary Eclipse spectrometer with an excitation wavelength of 390 nm. The photoelectrochemical experiment was analyzed by an electrochemical system (SP-150, France).

Catalyst preparation

Synthesis of BiOI

BiOI flower-like nanoparticles were made according to a previously described proce-dure [53]. BiOI particles were synthesized by adding 0.98 g of $Bi(NO_3)_3 \cdot 5H_2O$ and 0.34 g of KI in the 30 ml of ethylene glycol (EG) in a different vial. Next, KI solution was added slowly into the above solution, and stirred for 2 h.

After stirring to get a stable solution, the mixture was transferred into an autoclave for 18 h at 130 °C. Then, it was cooled down to room temperature. At last, the resulting precipitates were washed several times with ethanol and DI water and kept in an oven overnight at 80 °C.

Preparation of MIL-88A

The synthesis of MOF (MIL-88A) hexagonal microrods was performed via a hydro-thermal method [52]. $FeCl_3 \cdot 6H_2O$ (1.35 g) was dissolved in 15 ml of deionized (DI) water to which 0.87 g of fumaric acid dispersed in 20 ml of DI water was added.

After stirring for 2 h, the mixture was placed into a Teflon-lined stainless steel auto-clave and kept at 65 °C for 12 h. Finally, the resulting white product was washed with DI water and ethanol repeatedly and dried at 80 °C for 24 h in an oven.

Preparation of the MIL-88A/BiOI binary composite

The MIL-88A/BiOI structure was made by mixing 0.05 g of MIL-88A in 10 ml of EG under ultrasonication for 15 min. Next, 0.89 g of $Bi(NO_3)_3 \cdot 5H_2O$ dissolved in 15 ml of EG was diluted in the above solution while stirring. Subsequently, 0.33 g of KI dispersed in 15 ml of EG was added drop-wise to the prepared suspension under vigorous stirring for 60 min and stirred for 2 h at room temperature. The mixture was transferred into a 100-mL sealed Teflon-lined stainless steel autoclave for 18 h at 130 °C After completion of the reaction, the resulting product was separated by filtering and was washed with DI water and dried under vacuum at 50 °C overnight.

Evaluation of Photocatalytic activity

The photocatalytic activity of as-prepared samples was investigated by degradation of organic dyes under visible light irradiation at room temperature condition. The sample (0.01 g) was magnetically stirred in the dark for 20 min to establish the adsorption–desorption equilibrium, Then, the mixture was irradiated by a 300-W xenon lamp with suitable cutoff filters ($\lambda < 420$ nm). The photoreactor setup was completely explained in our previous article [29].

Result and discussion

Structural and morphological characteristics of photocatalysts

XRD analysis

The crystalline phase of the materials was verified by XRD analysis. The XRD patterns of BiOI, MIL-88A and MIL-88A/BiOI are exhibited in Fig. 1. The XRD pattern shows that the MIL-88A structure remained stable during the in situ synthesis of BiOI. The original BiOI exhibits the main diffraction peaks centered at 24.37°, 29.73°, 31.72°, 45.46° and 55.18°, and strong peaks of MIL-88A are shown at 8°, 10.4° and 12.9°. There were no extra peaks in the composite, indicating the high purity of the samples [54, 56]. Moreover, the main peaks of the BiOI were correctly deposited on the MIL-88A surface without any change. Besides, hardly any of the MIL-88A peaks appeared in the MIL-88A/BiOI nanocomposite. Also, the low content of MIL-88A and the high crystallinity diffraction peaks of BiOI were the main reasons for the disappearance of peaks in XRD measurement.
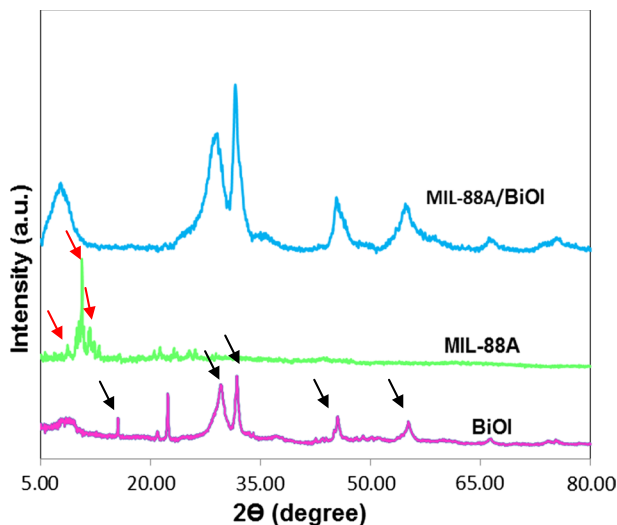
Fig. 1 X-ray diffraction patterns of prepared materials
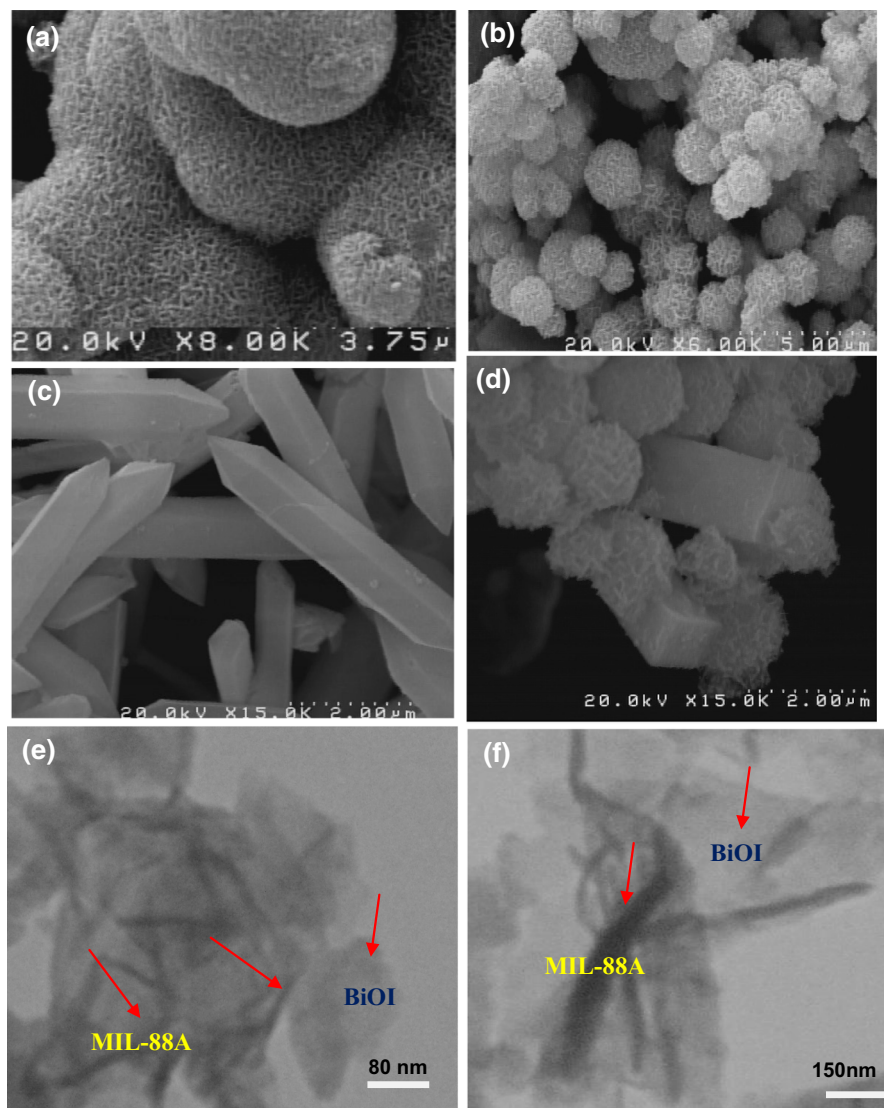
SEM and TEM images

To investigate of the morphology of the obtained materials, they were analyzed via field emission scanning electron microscopy (FE-SEM; Fig. 2). The SEM image of pure BiOI exhibits a flower-like morphology and uniform pore size ranging from ~ 1 μm to ~ 2 μm (Fig. 2a, b) [57]. As can be observed, the bare MIL-88A particles display hexagonal microrods; the nearly uniform diameter of MIL-88A is about 2 μm, as shown in Fig. 2c [52]. Also, FE-SEM images of the binary composite of MIL-88A/BiOI confirm a good coating with a porous MOF structure (Fig. 2c, d). Also, TEM images confirmed that BiOI particles were well distributed on the surface of MIL-88A, as indicated in Fig. 2e, f.

FT-IR spectroscopy

FT-IR spectra of MIL-88A, BiOI and MIL-88A/BiOI samples are given in Fig. 3. As observed, the strong peak at 489 cm^{-1} is attributable to the Bi–O stretching mode [58]. The Fe–O coordination peak at 575 cm^{-1} depends on Fe–O vibration of a MOF and the bands at 1396 cm^{-1} and 1603 cm^{-1} can be ascribed to the symmetric and asymmetric vibration modes of the C=O, respectively [56]. The broad peaks at 3300–3500 cm^{-1} correspond to the O–H stretching vibrations on the photocatalyst.

Electrochemical impedance spectroscopy measurements

EIS is a powerful technique for studying the electrochemical processes. Therefore, Fig. 4 shows impedance spectra of pure and composite structures and it

Fig. 2 SEM images of **a**, **b** BiOI, **c** MIL-88A, **d** MIL-88A/BiOI and TEM images of **e**, **f** MIL-88A/BiOI

can provide information about the charge transfer rate in photocatalytic activity. Figure 4 displays the Nyquist plots of the fabricated MIL-88A, BiOI and MIL-88A/BiOI at open-circuit potential (OCP) in the aqueous solution containing 10 mM $K_3[Fe(CN)_6]$:$K_4[Fe(CN)_6]$ (1:1) and 0.1 M KCl. The plots consist of an overall distorted semicircle which can be ascribed to the existence of double layers in the interface of samples with electrolyte. The diameter of the semicircle indicated total charge transfer resistance (R_{ct}) and ohmic resistance (R_s). As observed in Fig. 4, the hybridization of binary composite showed the highest electron transfer
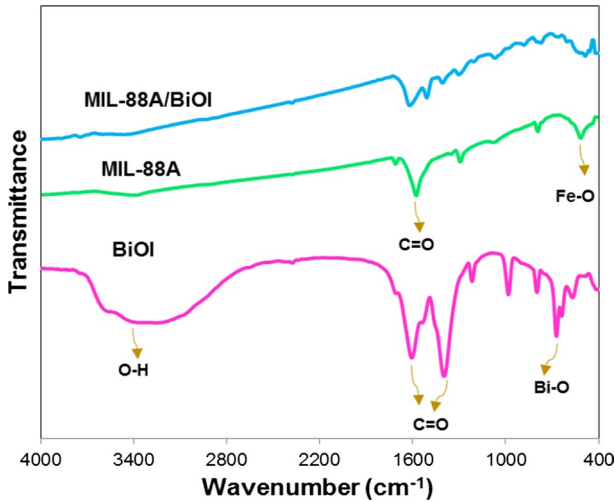
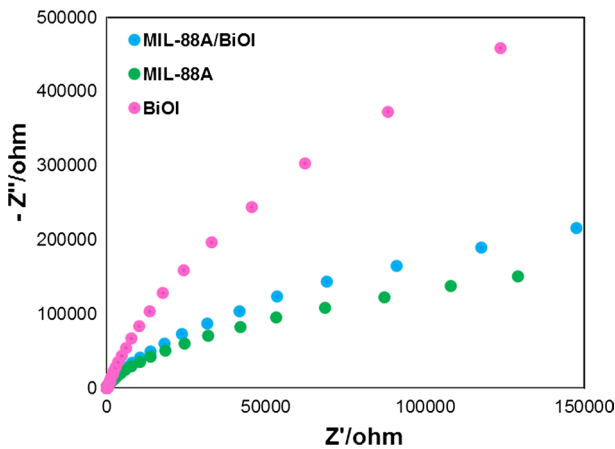**Fig. 3** FT-IR of as-prepared BiOI, MIL-88A and MIL-88A/BiOI materials

Fig. 4 EIS of samples in the presence of $K_3[Fe(CN)_6]:K_4[Fe(CN)_6]$ (1:1)

rate, suppressing the recombination of photogenerated electron/hole (e^-/h^+) pairs [55]. Thus, this can advance the photocatalytic performance via increasing the interfacial charge transfer and improve the rate of degradation of organic dyes.

Diffuse reflectance spectroscopy analysis

The light photoabsorption ability of as-synthesized materials was given by the UV–Vis absorption spectrum (Fig. 5). BiOI shows a band at 570 nm that is promising for visible light absorption, whereas, the MOF sample as a support material just displayed a weak peak in the visible light region. The spectral emission response of

the MOF shifted from a weak peak in the visible light region to strong peak in the visible light region of BiOI. So, the spectra of the binary composite displayed a red shift in the visible light region compared to the pure MIL-88A. Practical band gap values of BiOI and MIL-88A are about 1.78 eV and 2.05 eV, respectively [59].

Nitrogen adsorption analysis

Figure 6 shows N_2 adsorption/desorption isotherms of BiOI and MIL-88A/BiOI nanocomposite. The practical results show that the specific surface area for the bare BiOI is 78.1 m^2/g and 62.81 m^2/g for the MIL-88A/BiOI nanocomposite. The major reason for the great specific surface area of BiOI is that the high viscosity of glycol slows the reaction of $Bi(NO_3)_3.5H_2O$ and KI, and promotes the growth of BiOI in the form of nanosheets [60]. The high S_{BET} provided more reaction sites for degradation of organic dyes. BiOI nanosheets successfully grown on the surface of the MIL-88A and BiOI hierarchical structure further (diameter around 10 nm) deposit on the nanosheets. Moreover, the pore size distribution shows that the pores of all samples were distributed in the range of $0-50$ nm, matching with the mesoporous structure. Although the specific surface area of MIL-88A/BiOI is lower than that of BiOI, it is higher than pure MIL-88A, demonstrating that MIL-88A/BiOI heterojunction enhances the abundant surface active sites and improves photoactivity.

PL emission spectra and photocurrent response

To obtain the mechanism for the recombination of photoinduced electrons and holes in the photocatalysts, the PL emission spectra of BiOI, MIL-88A and MIL-88A/BiOI composites were detected under an excitation wavelength of 390 nm
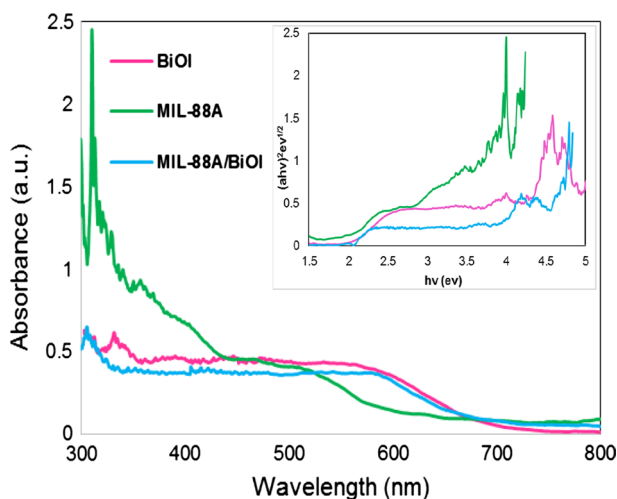

Fig. 5 UV–Vis diffuse reflectance spectra, and the calculated band gap energies of the MIL-88A, BiOI and MIL-88A/BiOI
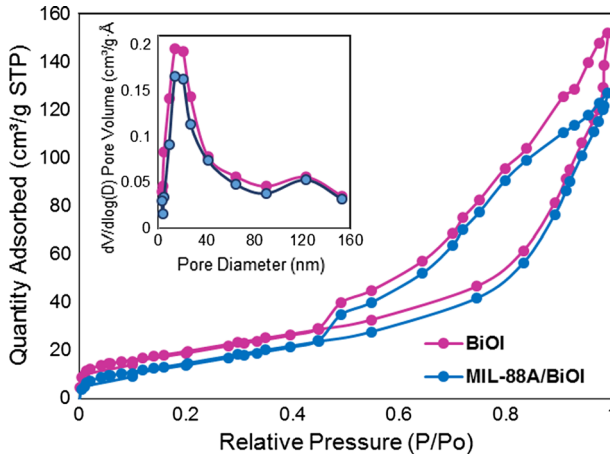
Fig. 6 N$_2$ sorption/desorption isotherms (the inset shows pore size distribution of BiOI and MIL-88A/BiOI)

(Fig. 7a). The PL spectra of samples show the major peak at 533 nm, which is mainly attributed to the recombination of free conduction band (CB) electrons and valence band (VB) holes. Also, PL analysis can be utilized to obtain the behaviors of e$^-$/h$^+$ pairs on trapping, immigration and charge transfer properties. The MIL-88A/BiOI exhibits lower PL intensity compared to pure BiOI. The practical result indicated that the BiOI decorates on MIL-88A, leading to weak recombination of electron/hole pairs, and higher photocatalytic activity which is adapted to the result of the photocatalytic experiment. These results show that MIL-88A/BiOI structure including oxygen vacancies and Z-scheme systems due to enhancing the degradation of organic dyes [61].
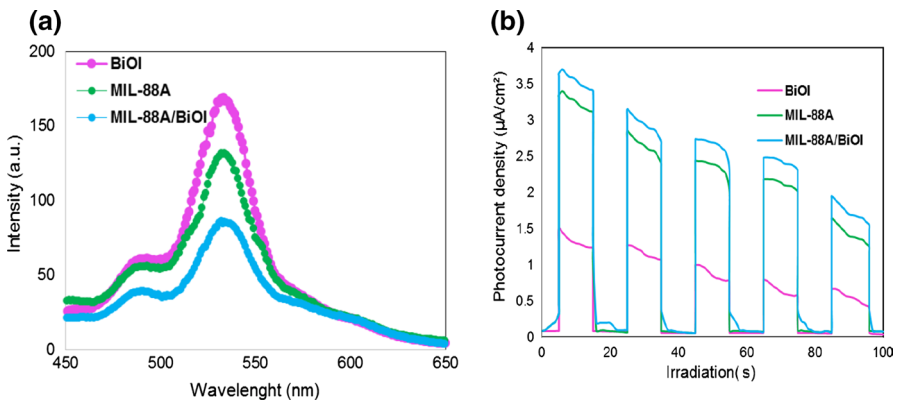
Fig. 7 PL spectra of different samples with the excitation wavelength of 390 nm (**a**), transient photocurrent curves of as-prepared materials (**b**)

Figure 7b displays the generated photocurrent of the as-prepared materials. It could be clearly seen that the photocurrent response from BiOI is significantly higher than MIL-88A sample under several on–off visible light irradiation cycles. It was generally shown that a larger photocurrent density illustrates a high-efficiency charge transfer and less recombination of photogenerated electron/hole pairs. The experimental result exhibits that when the lamp turns on, the photocurrent is raised sharply, and when turning off the light, the photocurrent quickly decreased to the initial condition. From the above results, the combination of MIL-88A and BiOI structures reaches a more efficient separation and transfer efficiency of photoinduced charge carriers with a higher photoactivity [62].

Photocatalytic experiments

Evaluation of the photocatalytic activity

Figure 8 shows the photodegradation performances of the synthesized samples. Dye (MB, AB92) degradation tests were comparatively carried out under visible light illumination. The degradation process was studied under different conditions. The solution mixture included organic dyes with photocatalyst stirred in the dark for half an hour. The experimental result in absence of any photocatalyst indicated the structure stability of organic dyes under visible light. It can be concluded that the degradation of both AB92 and MB occurs through photocatalysis. The essential steps for the best degradation are formation, migration and separation of photogenerated e^-/h^+ carriers. Clearly, without any light radiance, no e^-/h^+ pairs can be created. Thus, photocatalytic performance on the surface does not change. Pure BiOI and MIL-88A have indicated photocatalytic efficiency in the photodegradation process and they could degrade 50 and 22% and 20 and 12% of the AB92 and MB dyes, respectively, in 80 min under visible light. It is easily seen from Fig. 8 that the photoactivity MIL-88A was slightly less than that of BiOI. Moreover, after combining BiOI with MIL-88A, the photoactivity of the heterojunction was dramatically increased for the degradation of organic dyes; nearly 80% of AB92 and 45% of MB was degraded after 80 min of irradiation with visible light. So, MIL-88A/BiOI composite displayed the better performance for degradation of AB92 than that of MB. Thus, an efficient p–n junction between nanostructured MIL-88A and BiOI can play an important role to promote the separation efficiency of the charge carrier, increase interfacial charge transfer and enhance the photocatalytic activity of bare MIL-88A and BiOI.

Based on the experimental results, MIL-88A/BiOI structure shows remarkably enhanced photocatalytic activity via effective charge carrier separation and the decrease of the recombination rate (per EIS analysis) and the synergistic effect between MIL-88A and BiOI as a heterojunction.

According to DRS analysis results on the CB and VB of MIL-88A (0.03 and 0 eV vs. Normal hydrogen electrode (NHE)), the CB level of MIL-88A is higher than that of BiOI and could act as a sensitizer to absorb the visible light [26, 52]. Hence, the excited e^- on the CB of MIL-88A can be transmitted to the CB of BiOI, and the
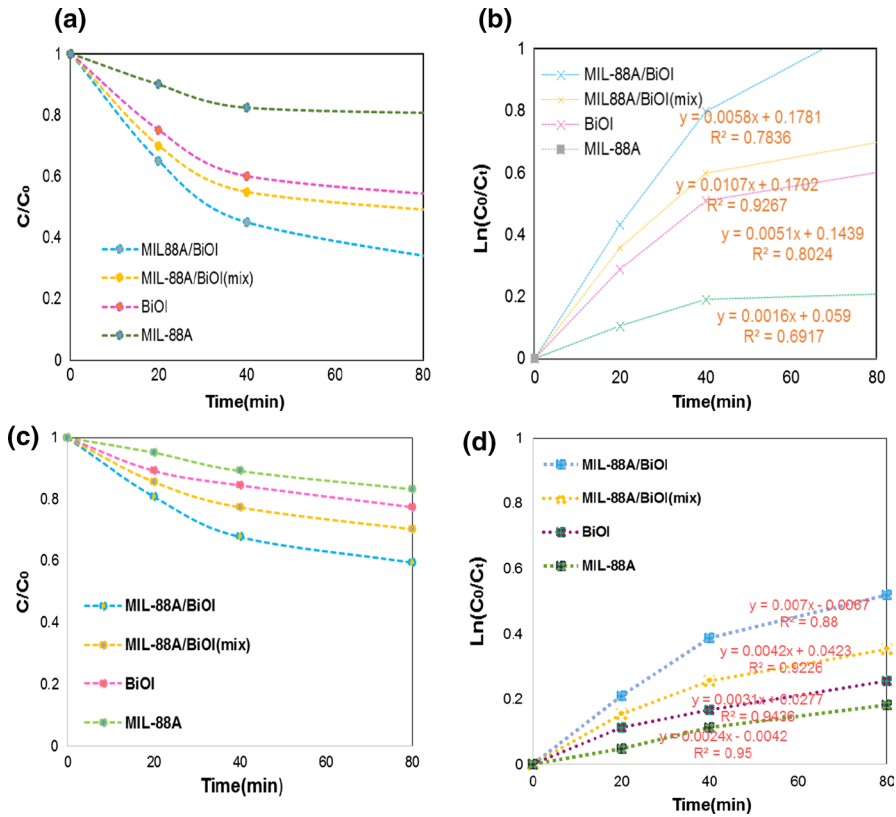
Fig. 8 The photodegradation activity for **a** AB92 and **c** MB and removal in the presence of obtained photocatalysts; **b** and **d** linear-log plot under visible light irradiation [65]

positive charge of VB level of BiOI can directly degrade organic molecules or react with OH⁻ to generate hydroxyl radical ($^\bullet$OH). The VB edge of BiOI shows that the photoexcited holes have a good oxidation capacity for degradation of organic dyes. These position levels in nano-heterostructure are suitable for induction of e^-/h^+ pairs in space efficiently and hinder the charge recombination (Fig. 9). Moreover, the crystallinity of Fe_3-μ_3-oxo cluster as Fenton-like reagents in the MIL-88A is responsible for the visible light absorption and the associated photoactivity. Fe-centered MIL-88A can be converted to the excited state of MOF* (MIL-88A*) under visible light. The photo-induced electrons in the ligand transfer to the Fe-oxo clusters, and obtains Fe^{2+}. The redox potentials of Fe^{3+}/Fe^{2+} are less than that of the CB, so the photo-induced electrons on the CB could be trapped and react with H_2O_2 to obtain $^\bullet$OH by Fenton-like excitation of H_2O_2 [52, 63]. Fe^{3+} was also utilized as reactant in the photocatalytic process to generate abundant and radical species ($^\bullet$OH and $^\bullet O_2^-$) which play a main role in enhancing the photoactivity for degradation of organic dyes. The generally accepted free radical-dominated chain reactions between Fe^{3+}/Fe^{2+} pair and H_2O_2 are shown below:
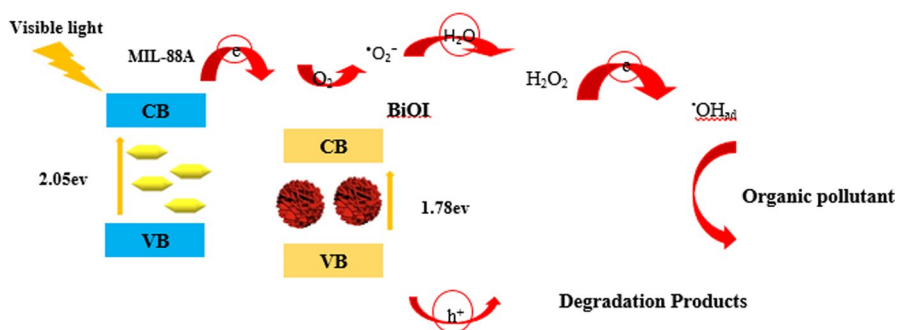
Fig. 9 Photoelectron transfer mechanism in the photodegradation of dyes over the MIL-88A/BiOI photocatalyst

$$Fe^{2+} + H_2O_2 \rightarrow Fe^{3+} + \cdot OH + OH^-$$

$$Fe^{3+} + H_2O_2 \rightarrow Fe^{2+} + \cdot O_2H + H^+$$
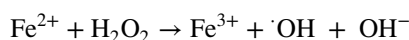
Based on the degradation efficiency results, MIL-88A/BiOI structure showed remarkably enhanced photocatalytic activity in comparison with the pure MIL-88A and BiOI. As can be seen, the MIL-88A/BiOI structure showed better photocatalytic degradation performance for anionic dyes (AB92) than for a cationic dye (MB). This is because the AB92 dye is much easier to adsorb on the positively charged nanocomposite than cationic dyes. It is clear that azo-dye of AB92 has a nitrogen double bond which is more active than MB. Moreover, in the reaction of radicals, the sulfonyl group in series of the para-substituted benzene ring in the molecule of the AB92 indicates more reactivity than sulfur connected in $=S+$ aromatic links in the molecule of the MB [29, 64].
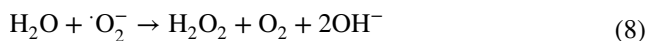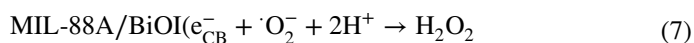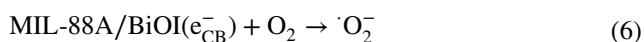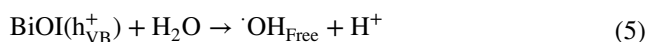
Kinetic analysis

The photodegradation reaction rate of dyes obeyed a pseudo-first order model, namely the Langmuir–Hinshelwood (L–H) kinetic. The proposed kinetic is confirmed by the equation of $\ln(C_0/C_t)^{1/4} = k_{app}t$, (1), in which C_0, C, t and k are concentration of photocatalyst at the initial time, concentration of photocatalyst after a specified time (mg L^{-1}), irradiation time (min) and reaction rate constant (min^{-1}), respectively [65, 66]. Figure 8 illustrates the reaction rate of organic dyes in the presence of MIL-88A/BiOI under visible light irradiation.

Effects of reactive species on organic dye photodegradation

To investigate the photodegradation mechanism of the photocatalyst, we also used the different scavengers to determine the main oxidant species, including 1,4-benzoquinone (BQ) which traps superoxide radicals, KI as a hole quencher (h^+) and hydroxyl radical ($\cdot OH$) and tert-butanol (t-BuOH) as scavengers of $\cdot OH$. As seen

in Fig. 9, the dye degradation greatly decreased in the presence of BQ as a superoxide anion scavenger, indicating that O_2 has a great potential to decompose the dyes. When 1 mmol of t-BuOH, acting as a $^\bullet$OH trap, was added to the mixture reaction, the dye concentration and color intensity was slightly changed. We can conclude that a few hydroxyl radicals were acting in the photodegradation of organic dyes. When 1 mmol of KI was added, the dye concentrations did not change, indicating the absence of H^+ species. Thus, $^\bullet O_2^-$ and $^\cdot$OH radicals play the major role as free radical oxidant species. Moreover, the quenching efficiency of BQ on radicals is more than that of t-BuOH, indicating $^\bullet O_2^-$ radicals can easily oxidize organic dyes. Based on the above results, the proposed mechanisms of light absorption follows in Eqs. (1)–(10) [29, 66].

$$\text{MIL-88A/BiOI} + \text{h}\upsilon \rightarrow \text{BiOI}(e_{CB}^- + h_{VB}^+) + \text{MIL - 88A}(e_{CB}^- + h_{VB}^+) \tag{1}$$

$$\text{MIL-88A/BiOI}(e_{CB}^-) + O_2 \rightarrow {}^\cdot O_2^- \tag{2}$$

$$\text{BiOI}(h_{VB}^+) + \text{Organic dyes} \rightarrow \text{Organic dyes}^{\cdot +} \tag{3}$$

$$\text{BiOI}(h_{VB}^+) + \text{OH}_{ads}^- \rightarrow {}^\cdot \text{OH}_{ads} \tag{4}$$

$$\text{BiOI}(h_{VB}^+) + H_2O \rightarrow {}^\cdot\text{OH}_{Free} + H^+ \tag{5}$$

$$\text{MIL-88A/BiOI}(e_{CB}^-) + O_2 \rightarrow {}^\cdot O_2^- \tag{6}$$

$$\text{MIL-88A/BiOI}(e_{CB}^- + {}^\cdot O_2^- + 2H^+ \rightarrow H_2O_2 \tag{7}$$

$$H_2O + {}^\cdot O_2^- \rightarrow H_2O_2 + O_2 + 2OH^- \tag{8}$$

$$H_2O_2 + \text{MIL-88A/BiOI}(e_{CB}^-) \rightarrow {}^\cdot\text{OH}_{ads} + OH^- + \text{MIL-88A/BiOI} \tag{9}$$

$$OH^- + h_{VB}^+ \rightarrow {}^\cdot\text{OH}_{ads} \tag{10}$$
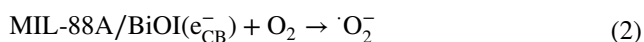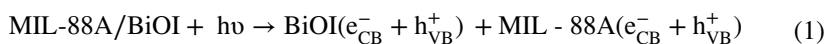
Based on the above results, it can be seen that CB (e^-) electrons were accumulated on the surface of MIL-88A/BiOI. In the presence of a scavenger, some of the electrons react with oxygen on the surface of the photocatalyst and are converted to a superoxide radical form. Furthermore, many electrons (e^-) react with H_2O to form H_2O_2. Electrons (e^-), H_2O_2 and $^\bullet\text{OH}_{ads}$ active species were involved in the degradation of the dyes (Fig. 10).

Conclusion

Novel MIL-88A/BiOI binary nanocomposite was designed, based on an Fe-based MOF and BiOI particles with effective band gap for enhancing the visible light response. Photocatalytic performance of the MIL-88A/BiOI composite was studied by decomposition of MB and AB92 under visible light irradiation. It is obvious that MIL-88A/BiOI nanocomposite has the highest activity compared to the pure samples. On the basis of extensive characterization of the electrical properties

Fig. 10 Effect of different scavengers on the degradation of **a** AB92 and **b** MB by MIL-88A/BiOI
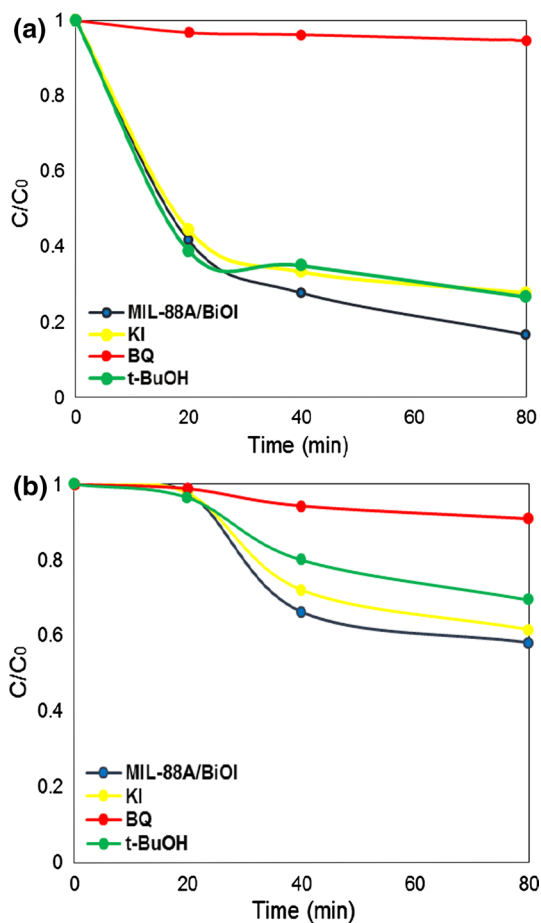
(EIS analysis), the electrical mobility of BiOI resulted in an efficient suppression of photogenerated charge carriers in the MIL-88A/BiOI. These outcomes display that the MIL-88A/BiOI heterojunction photocatalyst enhanced charge carriers, prolonging the lifetime and low recombination rate of the e^-/h^+ pairs. The kinetic results indicated that the AB92 and MB degradation obeys the pseudo-first-order reaction model as the L–H kinetic. The mechanism suggests that the $^\bullet OH$ and $^\bullet O_2^-$ radicals play the main roles in the photodegradation process.

References

1. E. Akbarrzadeh, M.R. Gholami, Res. Chem. Intermed. **43**, 5829 (2017)
2. S. Abdpour, E. Kowsari, MR. Moghadam, C. Janiak, L. Schmolke. J. Solid State Chem. (2018)
3. J. Chen, J. Cen, X. Xu, X. Li, Catal. Sci. Technol. **6**, 349 (2016)
4. S.Y. Moon, B. Naik, J.Y. Park, Korean J. Chem. Eng. **23**, 2533 (2016)
5. D. Liu D, W. Cai W, Y. Zhu, Appl. Catal B: Environ. 2018

6. G. Maxime, A.A. Amine, B. Abdelkrim, W. Dominique, Environ Sci and Pollut Res. **22**, 13127 (2014)
7. S. Cao, J. Low, J. Yu, M. Adv. Mater. **13**, 2150 (2015)
8. H. Salari, S.G. Khasevani, S.R. Setayesh, M.R. Gholami, Mater. Res. Innovations **22**, 137 (2016)
9. J. Di, J. Xia, Y. Ge, H. Li, H. Ji, H. Xu, Q. Zhang, H. Li, M. Li, Appl Catal B: Environ. **168**, 51 (2015)
10. J. Liang, F. Liu, J. Deng, M. Li, M. Tong, Water Res. **123**, 632 (2017)
11. M. Yan, Y. Hua, F. Zhu, W. Gu, J. Jiang, H. Shen, W. Shi, Appl Catal B: Environ. **202**, 518 (2017)
12. F. Deng, Q. Zhang, L. Yang, X. Luo, A. Wang, S. Luo, D.D. Dionysiou, Appl. Catal. B: Environ. (2018)
13. X. Xiao, W.D. Zhang, J. Mater. Chem. **28**, 5866 (2010)
14. C. Zhou, J. Cao, H. Lin, B. Xu, B. Huang, S. Chen. **272**, 213 (2015)
15. S. Gao, C. Guo, S. Hou, L. Wan, Q. Wang, J. Lv, Y. Zhang, J. Gao, W. Meng, G. Xu, J. Hazard. Mater. **33**, 11 (2017)
16. S. Petrović, Stojadinović, L. Rožić, N. Radić, B. Grbić, R. Vasilić, Surf Coat Technol. **250**, (2015)
17. H. Huang, X. Han, X. Li, S. Wang, P.K. Chu, Y. Zhang, ACS appl. mater & interfaces. **7**, 482 (2015)
18. S. Yin, J. Di, M. Li, Y. Sun, J. Xia, H. Xu, W. Fan, H. Li, J. Mater. Sci. **10**, 4769 (2016)
19. S.K. Hussain, L.K. Bharat, J.S. Yu, J. Mater. Chem. C. **27**, 6880 (2017)
20. Z. You, Q. Shen, Y. Su, Y. Yu, H. Wang, T. Qin, F. Zhang, D. Cheng, H. Yang. N.J.C. **42**, 489 (2018)
21. X. Qu, Y. Yi, F. Qiao, M. Liu, X. Wang, R.H. Yang, Y. Meng, L. Shi, F. Du, Ceram. Int. **44**, 1348 (2018)
22. J. Jiang, H. Wang, X. Chen, S. Li, T. Xie, D. Wang, Y. Lin, J. Colloid Interface Sci of colloid and interface science. **494**, 130 (2017)
23. J. Wang, L. Tang, G. Zeng, Y. Deng, Y. Liu, L. Wang, Y. Zhou, Z. Guo, J. Wang, C. Zhang, Appl. Catal. B: Environ. **209**, 285 (2017)
24. F.A. Sofi, K. Majid, O. Mehraj, J. Alloy. Compd. **737**, 798 (2018)
25. L. Yosefi, M. Haghighi, S. Allahyari, Sep. Purif. Technol. **178**, 18 (2017)
26. J. Cao, B. Xu, H. Lin, B. Luo, S. Chen, DaltonTrans. **37**, 11482 (2012)
27. D. Wu, H. Wang, C. Li, J. Xia, X. Song, W. Huang, Surf. Coat. Technol. **258**, 672 (2014)
28. M.J. Islam, D.A. Reddy, N.S. Han, J. Choi, J.K. Song, T.K. Kim, Phys. Chem. Chem. Phys. **36**, 24984 (2016)
29. S. Gholizadeh khasevani, N. Mohaghegh, M.R. Gholami, N. J. C. **41**, 10390 (2017)
30. M.J. Islam, H.K. Kim, D.A. Reddy, Y. Kim, R. Ma, H. Baek, J. Kim, T.K. Kim, Dalton Trans. **18**, 6013 (2017)
31. Z. Sha, J. Wu, Rsc Ad. **49**, 39592 (2015)
32. L. Shi, T. Wang, H. Zhang, K. Chang, X. Meng, H. Liu, J. Ye, Adv. Sci. **2**, 1500006 (2015)
33. M. Ma, A. Bétard, I. Weber, N, S, Cryst. Growth. Des. 13, 2286 (2013)
34. M.B. Chambers, X. Wang, L. Ellezam, O. Ersen, M. Fontecave, C. Sanchez, L. Rozes, C. Mellot-Draznieks, ACS. **139**, 8222 (2017)
35. D. Alezi, Y. Belmabkhout, M. Suyetin, P.M. Bhatt, J. Weseliński Ł, V. Solovyeva, K. Adil, I Spanopoulos, P.N. Trikalitis, A.H. Emwas, M.Eddaoudi. J.ACS. **41**, 1831 (2017)
36. K.J. Hartlieb, D.P. Ferris, J.M. Holcroft, I. Kandela, C.L. Stern, Y.Y.Botros Nassar, J.F. Stoddart, Mol. Pharmaceutics. **5**, 1831 (2017)
37. K.N. Chappanda, O. Shekhah, O. Yassine, S.P. Patole, M. Eddaoudi, K.N. Salama, Sens Actuators B Chem. **257**, 609 (2018)
38. B.J. Yao, L.G. Ding, F. Li, J.T. Li, Q.J. Fu, Y. Ban, A. Guo, Y.B. Dong, ACS Appl. Mater. Interfaces. **44**, 38919 (2017)
39. W. Huang, N. Liu, X. Zhang, M. Wu, L. Tang. **425**, 107 (2017)
40. X. Zhang, H. Li, X. Lv, J. Xu, Y. Wang, C. He, N. Liu, Y. Yang, Y. Wang. Chem. Eur. J. (2018)
41. X. Zhang, L. Song, F. Hou, Y. Yang, Y. Wang, N. Liu, Int J Hydrogen Energ. **43**, 18279 (2018)
42. Y. Wang, Y. Yang, N. Liu, Y. Wang, X. Zhang, RSC Adv. **58**, 33096 (2018)
43. I. Majeed, M.A. Nadeem, A. Badshah, K. Anodarwala, H. Ali, M.A. Khan, J.A. Stride, M.A. Nadeem, Catal. Sci. Technol. **3**, 677 (2017)
44. X. Zhang, F. Hou, Y. Yang, Y. Wang, N. Liu, D. Chen, Y. Yang, Appl. Surf. Sci. **423**, 771 (2017)
45. X. Zhang, F. Hou, H. Li, Y. Yang, Y. Wang, N. Liu, Y. Yang, Microporous Mesoporous Mater. **15**, 211 (2018)
46. X. Zhang, Y. Yang, L. Song, Y. Wang, C. He, Z. Wang, L. Cui, Mol. Catal. **447**, 80 (2018)

47. K.Y. Lin, F.K. Hsu, Rsc Adv. **63**, 50790 (2015)
48. X. Zhang, H. Li, F. Hou, Y. Yang, H. Dong, N. Liu, Y. Wang, L. Cui, Appl. Surf. Sci. **411**, 27 (2017)
49. X. Zhang, Y. Yang, W. Huang, Y. Yang, Y. Wang, C. He, N. Liu, M. Wu, L. Tang, Mater. Res. Bull. **99**, 349 (2018)
50. Z.D. Lei, Y.C. Xue, W.Q. Chen, L. Li, W.H. Qiu, Y. Zhang, L. Tang, Small **35**, 1802045 (2018)
51. N. Liu, W. Huang, X. Zhang, L. Tang, L. Wang, Y. Wang, M. Wu, APPL CATAL B-ENVIRON. **221**, 119 (2018)
52. W.T. Xu, L. Ma, F. Ke, F.M. Peng, G.S. Xu, Y.H. Shen Y, J.F. Zhu, L.G. Qiu, Y.P. Yuan, Dalton Trans. **43**, 3792(2014)
53. J. Hu, S. Weng, Z. Zheng, Z. Pei, M. Huang, P, J. hazard. Mater. **15**, 293 (2014)
54. K. Dai, L. Lu, C. Liang, G. Zhu, Q. Liu, L. Geng, J. He, Dalton Trans. **44**, 7903 (2015)
55. L. Ye, X. Liu, Q. Zhao, H. Xie, L. Zan, J. Mater. Chem. A. **1**, 8978 (2013)
56. J. Wang, J. Wan, Y. Ma, Y. Wang, M. Pu, Z. Guan, RSC. Adv. **6**, 112502 (2016)
57. C. Chang, L. Zhu, S. Wang, X. Chu, L. Yue, ACS. Appl. Mater Interfaces **6**, 5083 (2014)
58. Y. Zhou, S. Fang, M. Zhou, G. Wang, S. Xue, Z. Li, S. Xu, C. Yao, J. Alloy. Compd. **696**, 353 (2017)
59. Y. Tong, C. Zheng, W. Lang, F. Wu, T. Wu, W. Luo, H. Chen, Mater. Design. **122**, 90 (2017)
60. J. Hou, K. Jiang, M. Shen, R. Wei, X. Wu, F. Idrees, C. Cao, Sci. Rep. **7**, 11665 (2017)
61. N. Liu, W. Huang, X. Zhang, L. Tang, L. Wang, Y. Wang, M. Wu, APPL CATAL B-ENVIRON. **221**, 119 (2018)
62. W. Huang, C. Jing, X. Zhang, M. Tang, L. Tang, M. Wu, N. Liu, Chem. Eng. J. **349**, 603 (2018)
63. X. Li, Y. Pi, L. Wu, Q. Xia, J. Wu, Z. Li, J. Xiao, Appl. Catal. B-Environ. **202**, 653 (2017)
64. C.C. Wang, J.R. Li, X.L. Lv, Y.Q. Zhang, G. Guo, Energ. Eniron. Sci. **9**, 2831 (2014)
65. X. Zhang, Y. Wang, F. Hou, H. Li, Y. Yang, X. Zhang, Y. Yang, Y. Wang, Appl. Surf. Sci. **391**, 476 (2017)
66. J. Hong, C. Chen, F.E. Bedoya, G.H. Kelsall, D. O'Hare, C. Petit, Catal. Sci. Technol. **6**, 5042 (2016)